Langmuir

Article

pubs.acs.org/Langmuir

Combining Colloidal Probe Atomic Force and Reflection Interference Contrast Microscopy to Study the Compressive Mechanics of Hyaluronan Brushes

Seetharamaiah Attili[†,‡] and Ralf P. Richter*[,†,‡]

[†]Biosurfaces Unit, CIC biomaGUNE, Paseo Miramon 182, 20009 Donostia−San Sebastian, Spain

[‡]Max-Planck-Institute for Intelligent Systems, Heisenbergstrasse 3, 70569 Stuttgart, Germany

ABSTRACT: We describe a method that combines colloidal probe atomic force microscopy (AFM) and reflection interference contrast microscopy (RICM) to characterize the mechanical properties of thin and solvated polymer films. When analyzing polymer films, a fundamental problem in colloidal probe AFM experiments is to determine the distance at closest approach between the probe and the substrate on which the film is deposited. By combining AFM and RICM in situ, forces and absolute distances can be measured simultaneously. Using the combined setup, we quantify the compressive mechanics of films of the polysaccharide hyaluronan that is end-grafted to a supported lipid bilayer. The experimental data, and comparison with polymer theory, show that hyaluronan films are well-described as elastic, very soft and highly solvated polymer brushes. The data on these well-defined films should be a useful reference for the investigation of the more complex hyaluronan-rich coats that surround many living cells.

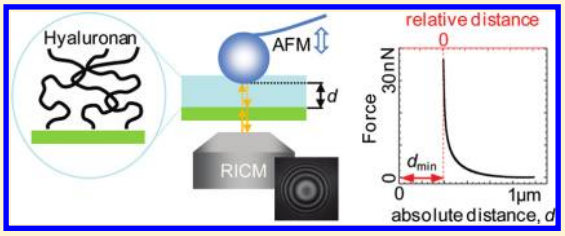

INTRODUCTION

Highly solvated polymer films have naturally evolved as multifunctional interfaces in a number of biological systems, for example as mucosal films in the lungs and the gastrointestinal or reproductive tracts, as cellular coats around many cells[1] or in bacterial biofilms. Surface-confined polymer films are also becoming increasingly popular in a variety of applications in (bio)technology, as antifouling[2] or low-friction coatings,[3] for colloidal stabilization, as substrates for cell culture,[4] in biomaterials, for sensing, etc.[5] To generate such polymer films, individual polymer chains are attached to or grown from surfaces, in one or multiple steps to form a single or multiple layers. Attachment can occur either via multiple contact points along the polymer chain or via one of the chain ends. In the latter case, and if the chains are grafted at sufficiently high density, repulsion between chains induces the formation of a so-called polymer brush.[6,7] In addition, the polymer chains may be interconnected by covalent or more transient noncovalent interactions, forming (hydro)gel films.

The mechanical response of such polymer films is not only important for functional performance, but it can also provide valuable information about their internal organization, interactions and dynamics. Colloidal probe atomic force microscopy (AFM)[8,9] is a popular and versatile technique for investigating the mechanical properties of thin films and macroscopic materials.[10−13] It measures the forces, with pN resolution, that act on a nanometer or micrometer-sized spherical probe as it interacts with the material of interest. In the case of thin polymer films, it is often desirable to be able to relate the response to compression or shear forces to the film's thickness and to the precise location of the probe within the film. Ideally, one would want to measure the *absolute* distance between the probe and the solid substrate at the same time as the probe interacts with the film. A fundamental limitation of colloidal probe AFM is that the distance between the surfaces is not measured explicitly but inferred from the force measurement. For the characterization of polymer films, the consequence is that only *relative* changes in distance are accessible to experiment whereas the *absolute* probe-substrate distance remains unknown. In some cases, the probe-substrate distance can be inferred indirectly. For example, film thickness can be estimated by local removal (scratching) of the film with the aid of the AFM probe and subsequent analysis of the scratch depth.[14] This method though bears the risk of contaminating or even damaging the AFM probe. Patterned surfaces, in which the film and the bare surface are presented side by side,[15] provide useful means to perform reference measurements in the immediate vicinity of the film, from which the film thickness can then be deduced. This approach, however, requires surface functionalization methods that are not always easily applicable, e.g., for films that are built on supported lipid bilayers containing laterally mobile lipids.

Optical techniques such as reflection interference contrast microscopy (RICM) or total internal reflection microscopy present an interesting way to determine the distance between a colloidal probe and a planar substrate, because they can be used in a liquid environment and are compatible with AFM.[16] RICM in particular can provide absolute distances with a resolution of a few nanometers and detect small-scale distance fluctuation with down to sub-Angstrom precision.[17−21] Here, we present a novel method that combines AFM and RICM in situ

Received: November 22, 2011
Revised: December 27, 2011
Published: January 4, 2012

   dx.doi.org/10.1021/la204602n | *Langmuir* 2012, 28, 3206−3216

to quantify the interaction forces between a colloidal probe and a (coated) planar substrate as a function of their absolute distance. With the ability to measure forces and absolute distances simultaneously, the method resembles another well-known technique, the surface force apparatus (SFA, reviewed in ref 22). This method, although demanding and mastered by only a few research groups worldwide, has over the past three decades been very successfully used for the investigation of forces between surfaces and surface-confined polymer films.[3,23,24] With the commercial availability of combined atomic force and optical microscopy, AFM and RICM can now be quite easily combined into one instrument,[25−29] and the approach that we propose can hence in the future be readily adopted by many research groups.

Biological polymer films that are of particular interest to our own research and triggered our technological development are the very soft and strongly hydrated coats that are rich in the glycosaminoglycan hyaluronan (HA) and that surround many types of cells.[1,30] Such pericellular coats (PCCs) can be between 100 nm and many micrometers thick, influence vital cellular processes and play important roles in physiological and pathological processes, such as inflammation, fertilization,[31] embryogenesis,[32] tumor development, osteoarthritis and atherosclerosis.

HA is a linear polymer of disaccharides. At physiological pH, the disaccharides are negatively charged (pK_a ~3).[33] Each disaccharide has a length of 1 nm, and is made of glucuronic acid and *N*-acetylglucosamine. Extracellular HA typically has a molecular weight of a few million Daltons,[32] i.e. a contour length of several micrometers. HA serves as a versatile polymeric scaffold within which other molecules are organized and regulated. A variety of proteins, called hyaladherins, can bind to the flexible HA chains and engender self-assembly into large hydrogel-like multimolecular architectures.[30,34−36] To study the relationships between composition, supramolecular structure and dynamics, physicochemical properties, and biological function of HA assemblies, we have recently developed films of HA chains that are grafted with one of their ends to a supported lipid bilayer as a tailor-made model system of PCCs (Figure 1B).[20]

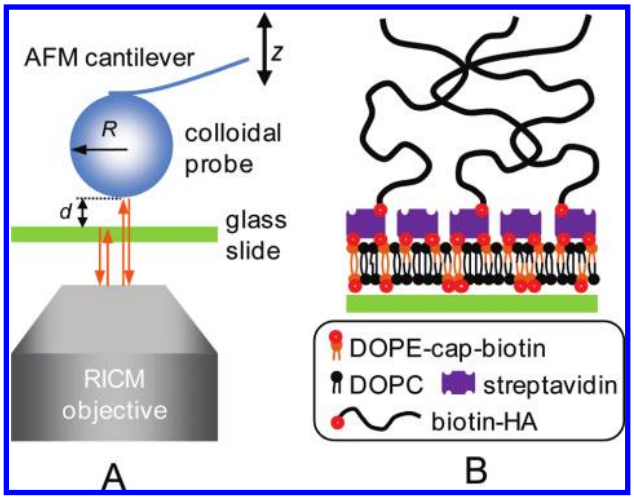

Figure 1. (A) Scheme of the combined colloidal probe AFM/RICM setup. (B) Scheme of the architecture of HA films. The size of streptavidin and the thickness of the supported lipid bilayer are drawn to scale; the mean anchor spacing and contour length of HA, and the thickness of the HA film are further reduced in size for illustrative purposes.

In this model system, the HA molecular weight is well-controlled, and the physicochemical properties of the HA films as a function of external cues become accessible to quantitative investigation by surface-sensitive biophysical techniques.[20,36] To our knowledge, the mechanical properties of end-grafted HA films have not yet been explored.

In the first part of this paper, we describe the details of the method of combining colloidal probe AFM and RICM to measure forces as a function of absolute probe-substrate distance. In the second part, we apply the technique to investigate the compressive response of end-grafted HA films.

MATERIALS AND METHODS

Combined Colloidal Probe AFM and RICM Setup. We used a NanoWizard II (JPK, Berlin, Germany), installed on an inverted optical microscope (Axio Observer D1; Zeiss, Oberkochen, Germany) to combine colloidal probe AFM and RICM (Figure 1A). The NanoWizard II was equipped with an *x* and *y* sample scanner (TAO module; JPK), which enables force measurements at various spots on a given sample while maintaining the colloidal probe aligned along the optical axis of the microscope. AFM force curves were acquired in closed-loop mode at an approach speed of v_{piezo} = 100 nm/s, and with a maximal load on the order of typically 10 nN.

The optical microscope was equipped with a mercury lamp (X-Cite 120; Lumen Dynamics Group, Ontario, Canada) as light source in epi-illumination reflection mode. Stray light was filtered by the antiflex technique,[37] using a filter cube with crossed polarizers (AHF Analysentechnik, Tübingen, Germany) and an antiflex oil-immersion objective (EC Plan Neofluar Antiflex, 63×/1.25; Zeiss).[19,38] The colloidal probe was aligned to the optical axis with the aid of the bright field transmission optics of the optical microscope, and approached to the sample surface by the AFM stepper motors, until the characteristic Newtonian fringe pattern (Figure 2A) started to appear in RICM imaging mode. The emergence of the fringe pattern indicated that the probe was within a distance of a few μm from the sample. To optimize the quality of the RICM image, the opening of the field diaphragm was adjusted. The opening of the aperture diaphragm was kept minimal and constant throughout all measurements. Interferographs at 438 and 543 nm were acquired simultaneously by two halves of the same chip (1344 × 1024 pixels) of a CCD camera (ORCA-ER, Hamamatsu Photonics, Massy, France) (Figure 2A-B). To this end, the beam of reflected light exiting the microscope was guided through a custom-built beam splitter and filter unit. The unit contained (i) a chromatic beam splitter to separate light above and below 505 nm (Q505LP; AHF Analysentechnik), (ii) two bandpass filters of around 20 nm width, centered at wavelengths of λ = 438 and 543 nm, respectively (BrightLine HC 438/24 and BrightLine HC 543/22; AHF Analysentechnik), and (iii) two mirrors, focusing lenses and a laser beam splitter (600DCR; AHF Analysentechnik) to guide the two filtered beams onto the camera chip at a resolution of typically 50 nm per pixel. Images were acquired at a frame rate of 8 s^{-1} using the software SimplePCI (Hamamatsu) and an exposure time of 100 ms. A set of about 100 interferographs were acquired per AFM force curve.

Substrate Preparation. Glass coverslips (no. 1.5, 24 × 24 mm^2; Menzel-Gläser, Thermo Scientific, Germany) were cleaned by rubbing with a lint-free tissue paper and immersion in freshly prepared piranha solution (a 3:1 (*v*/*v*) mixture of concentrated H_2SO_4 and 50% H_2O_2) for 1 h, rinsed thoroughly with ultra pure water, and gently blow-dried with a stream of N_2 gas. Substrates were stored in sealed Petri dishes. Prior to use, the glass coverslips were treated with UV/ozone

dx.doi.org/10.1021/la204602n | *Langmuir* 2012, 28, 3206−3216

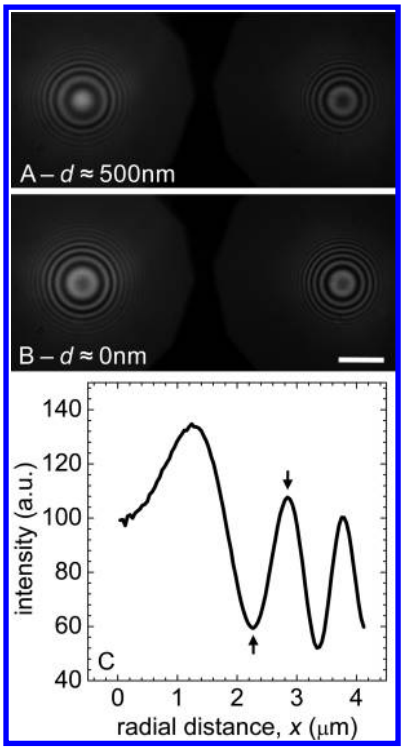

Figure 2. RICM data. (A and B) Dual wavelength interferographs at λ = 543 (left) and 438 nm (right) of a colloidal probe that was attached to an AFM cantilever and positioned at a distance of approximately 500 nm from a clean glass surface (A) and in close proximity to the surface (B). The characteristic set of concentric rings (Newtonian rings) is formed by the interference of light beams that are reflected at the glass/liquid and liquid/probe interfaces, respectively. A part of the edges of the field diaphragm that are used to focus the image are visible in the image centers. Scale bar: 5 μm. (C) Representative radially averaged intensity profile (λ = 543 nm) computed from the Newtonian rings in B (left). Two extrema that were used for the determination of the probe-surface distance d according to the R-adjustment method are marked (arrows).

(UV/Ozone ProCleaner; Bioforce Nanoscience, Ames, IA, U.S.A.) for 30 min.

Preparation of Colloidal AFM Probes. Polystyrene microspheres (Polysciences, Eppelheim, Germany) of 25 ± 3 μm diameter (sizes provided by the manufacturer) were attached to tipless V-shaped Si_3N_4 cantilevers with a nominal spring constant of 0.06 N m^{-1} (Veeco Probes, CA, U.S.A.), using a black two-component epoxy glue (EPO-TEK 320, Polytec GmbH, Waldbronn, Germany). The real cantilever spring constant, determined before attaching the microsphere using the thermal noise method,[39] was k = 0.1 N m^{-1}. The microspheres were washed in ethanol and in ultra pure water and stored in ultra pure water at 4 °C. Before use, they were transferred into ethanol, 5 μL of the solution was spread on a cleaned glass coverslip, and the ethanol was left to evaporate. A small droplet of about 1 μL of epoxy glue mixture was deposited on the same glass slide. The glass coverslip was mounted on an inverted microscope with 20× objective. A micromanipulation setup was used to wet the end of a given AFM cantilever with glue and to attach a single microsphere to its apex. We found the gluing procedure to give the best results if the epoxy mixture was left to viscosify for about 1 h before use. Care was taken to wet a sufficient part of the lower cantilever face with the black glue (to avoid undesired reflections from the bottom of the cantilever during RICM imaging) but not to coat the upper Au-coated face (which is crucial for the laser-based detection of the cantilever bending in the AFM). Prior to use, the cantilevers with colloidal probe were treated with UV/ozone for not more than 5 min.

Preparation of the Liquid Chamber. A cleaned glass coverslip was first attached to a custom-made titanium sample holder using two-component glue (Twinsil; Picodent, Wipperfurth, Germany) and covered with a droplet of 250 μL of aqueous solution. The desired biomolecular film was prepared on the substrate, and the sample was installed on the AFM sample stage. The sample holder was designed to accommodate both a liquid cell (SmallVolumeCell; JPK) on the top and a light microscope objective on the bottom. A chip with a colloidal probe cantilever was glued to the liquid cell using Twinsil glue. For measurements with liquid exchange, the liquid cell was equipped with silicone tubings and with a silicone rubber ring (closed liquid cell). The sample holder, the liquid cell, the tubings, and the silicone rubber ring were cleaned by sonication, first in ethanol and then in ultra pure water, for 30 min, respectively. The accessories were rinsed thoroughly with ultra pure water after each sonication step and eventually blow-dried with a stream of N_2 gas. The liquid cell was mounted on the AFM head, and the tubings and the liquid cell were filled with aqueous solution using a pair of syringes, until a hanging droplet was formed in the liquid cell. The AFM head was then mounted on the AFM sample stage and lowered toward the sample using stepper motors until the silicon rubber ring made a good seal with the glass substrate. Care was taken to avoid bubbles and to keep the sample wet at all times. For further exchange of liquids, the inlet port of the liquid cell was connected to a peristaltic pump (Ismatec, Glattbrugg, Switzerland). Applied flow rates were typically 0.5 mL/min. For measurements without liquid exchange, the liquid cell was used without tubings and rubber ring (open liquid cell), and liquid was filled into the inlet and outlet ports of the liquid cell with the aid of a pipet.

Preparation of Lipid Vesicles, Streptavidin, and Hyaluronan. Lyophilized dioleoylphosphatidylcholine (DOPC) and dioleoylphosphatidylethanolamine-CAP-biotin (DOPE-CAP-biotin) (Avanti Polar Lipids, Alabaster, AL, U.S.A.) were dissolved in chloroform, mixed in a molar ratio of 9:1, dried, resuspended in buffer (10 mM HEPES, pH 7.4, 150 mM NaCl, 3 mM NaN_3), and homogenized, as described earlier.[40] Small unilamellar vesicles (SUVs) of 2 mg/mL concentration were obtained by sonication, as described earlier[41] and stored at 4 °C.

Lyophilized hyaluronan (HA), biotinylated at its reducing end and with a well-defined molecular weight of 1.08 ± 0.06 MDa was purchased from Hyalose (Select-HA B1000; Oklahoma City, OK, U.S.A.). HA was dissolved in ultra pure water at a concentration of 1 mg/mL, and gently shaken for 2 h. The stock solution was aliquoted, and stored at −20 °C. Lyophilized streptavidin (Sigma) was dissolved in ultra pure water at a concentration of 1 mg/mL and stored at −20 °C.

Preparation of HA Films. Films of grafted HA (Figure 1B) were prepared within a 250 μL droplet of buffer solution (10 mM HEPES, pH 7.4, 150 mM NaCl, 3 mM NaN_3) on the glass coverslip, adapting a previously described method.[20] First, SUVs were added at a final concentration of 100 μg/mL together with 2 mM $CaCl_2$ and incubated for 30 min. Second, streptavidin was incubated at 20 μg/mL for 30 min. Third, biotinylated HA was incubated at 20 μg/mL for 8 h. To remove the excess sample after each incubation step, the droplet content was diluted by repeated addition of a 2-fold excess of buffer and removal of excess liquid until the concentration of the solubilized sample, estimated from the extent of dilution, was below 10 ng/mL. Repeated aspiration and release of the

dx.doi.org/10.1021/la204602n | Langmuir 2012, 28, 3206−3216

droplet content by a micropipet ensured homogenization of the cuvette content at each dilution step. Care was taken to keep the substrate wet at all times.

RESULTS

Combined Colloidal Probe AFM/RICM Measurements.

The combined AFM/RICM setup is schematically shown in Figure 1A. The AFM was operated in conventional force mode: the cantilever was first approached toward and then retracted from the sample surface at a constant speed by the *z*-piezo, and the AFM's laser detection system recorded changes in the deflection of the cantilever. At the same time, a series of dual-wavelength RICM images (representative images are shown in Figure 2, panels A and B) was taken.

Analysis of RICM Data. Different theoretical models have been reported in the past to extract the glass-probe distance d from RICM images.[18,19,21] For our purposes, we found the simplest model, the parallel plate approximation with incident light parallel to the surface normal,[18] most suitable. According to this model, d can be derived from the radial position of a selected extremum of the radially averaged intensity profile (a representative profile for λ = 543 nm is shown in Figure 2C) of the Newtonian ring pattern (Figure 2, panels A and B). In fact, multiple extrema provide multiple solutions, and detailed analysis reveals that the correlation of two carefully chosen solutions can be used (i) to reliably determine d without a priori knowledge of the exact probe radius and (ii) to correct for an imperfectly adjusted focus position. This method, which we call "*R*-adjustment", is described in detail below. Considering that colloidal probes typically exhibit a rather large variation in their diameter and that the accurate determination of the bead radius by light microscopy is not trivial (in particular for a probe attached to an AFM cantilever), the *R*-adjustment method simplifies data acquisition and evaluation, when compared to established methods.[19]

"R-adjustment" Method. We used a custom-developed algorithm, implemented in Matlab, to analyze RICM images. Each image was split into two halves, corresponding to interferographs at λ = 438 and 543 nm, respectively, and the two interferographs were analyzed independently. We use a set of interferographs at λ = 543 nm to demonstrate the analysis principle. First, the radially averaged intensity profiles of the Newtonian ring patterns was computed. A pattern for a selected interferograph is shown on the left side of Figure 2B, and the intensity profile in Figure 2C. The glass-probe distance, d, can be derived from the radial position, $x_{\mathrm{ext}}^{(i)}$, of a selected extremum, i, in the intensity profile[18]

$$d_{\mathrm{min}}^{(l)} = \frac{\lambda l}{2n} - R + \sqrt{R^2 - x_{\mathrm{ext}}^{(i)2}}$$

if the extremum i is a minimum (1A)

and

$$d_{\mathrm{max}}^{(l)} = \frac{\lambda(2l+1)}{4n} - R + \sqrt{R^2 - x_{\mathrm{ext}}^{(i)2}}$$

if the extremum i is a maximum (1B)

Here R is the probe radius, n is the refractive index of the aqueous medium between the probe and the glass surface (n = 1.334), and l is the fringe order (1, 2, ...).

According to the simple model and if l is selected properly, d should not depend on the choice of the extremum. Significant deviations are though expected to occur if the extremum is situated too far from the center, because corrections to the parallel plate approximation that arise from the finite curvature of the colloidal probe become important.[42] On the other hand, we observed that the accuracy in the determination of the extremum position decreased significantly for distances below 1.3 μm from the center, due to a limited number of pixels available for evaluation. For these reasons, we computed d only from the two extrema situated closest to but not closer than 1.3 μm from the center (arrows in Figure 2B). In the following, the radial positions of these extrema and the resulting distances will be denoted as $x_{\mathrm{ext}}^{(\mathrm{I})}$ and $x_{\mathrm{ext}}^{(\mathrm{II})}$ and as $d^{(\mathrm{I})}$ and $d^{(\mathrm{II})}$, respectively.

Figure 3A shows the evolution of $d^{(\mathrm{I})}$ and $d^{(\mathrm{II})}$, calculated from $x_{\mathrm{ext}}^{(\mathrm{I})}$ and $x_{\mathrm{ext}}^{(\mathrm{II})}$ in a series of RICM images with a nominal R = 12.5 μm, during the acquisition of an AFM force curve on a clean glass surface in the presence of 10 mM NaCl. Approach and retraction rates of 100 nm/s and an exposure time of 100 ms imply that each interferograph, and the calculated distances, represent averages over a probe travel of up to 10 nm. Initially, the distances decrease roughly linearly, as expected for approach at constant rate of the probe toward the surface. The plateau at intermediate times corresponds to "hard-wall" contact between colloidal probe and glass surface, and the linearly increasing part to the retraction at constant rate. Overall, the curves for $d^{(\mathrm{I})}$ and $d^{(\mathrm{II})}$ are quite similar, as expected. A plot of the differences $\Delta d = d^{(\mathrm{I})} - d^{(\mathrm{II})}$ (Figure 3B) though revealed significant deviations. In the particular measurement in Figure 3, panels A and B, Δd exhibited a mean value of 24 nm. Periodic variations in Δd with about 8 nm amplitude as a function of the probe-sample distance were also observed.

One parameter that had a strong influence on the deviations was R. Adjustment of R such as to minimize $\chi^2 = \sum_t \Delta d(t)^2$ (Figure 3, panels C and D) decreased the mean value to zero. It also decreased the amplitude of the periodic variations, albeit only weakly. The effective probe radius was found to be 15.6 ± 0.2 μm, where the error in R corresponds to the range within which χ^2 increased by less than 2-fold above its minimum.

Another parameter that we found to sensitively affect $d^{(\mathrm{I})}$, $d^{(\mathrm{II})}$, and Δd was the position of the focus of the microscope objective with respect to the sample. To quantify the impact of the focus position on our data, we acquired several series of RICM images while systematically varying the focus position within a range of ±3 μm around the optimal focus. Interestingly, the final values for $d^{(\mathrm{I})}$, $d^{(\mathrm{II})}$, and Δd for all image sets within the range of ±2 μm around the optimal focus agreed well, to within ±3 nm, after application of the above-described *R*-adjustment method (data not shown). Furthermore, the effective probe radius depended linearly on the focus position (Figure 3C, inset). These experimental results imply that variations in the focus position have the same effect as variations in the probe radius on the extrema positions in the radial intensity profiles of RICM images. We note in passing that the data for Figure 3A–D was intentionally acquired with too low a focus position, to better illustrate the method of *R*-adjustment. This explains why the effective probe radius is somewhat larger than the value specified by the manufacturer. Effective probe radii measured at optimal focus position agreed to within 500 nm with values estimated from bright field microscopy images taken prior to attachment of the probes to the AFM cantilever.

The periodic variations in Δd could not be completely removed by the *R*-adjustment method (Figure 3D). Within the ranges of constant approach or retract rate, the length of the period was approximately 2 s, corresponding to 200 nm in distance. The latter value matches the period $\lambda/2n$ of the RICM

dx.doi.org/10.1021/la204602n | Langmuir 2012, 28, 3206–3216

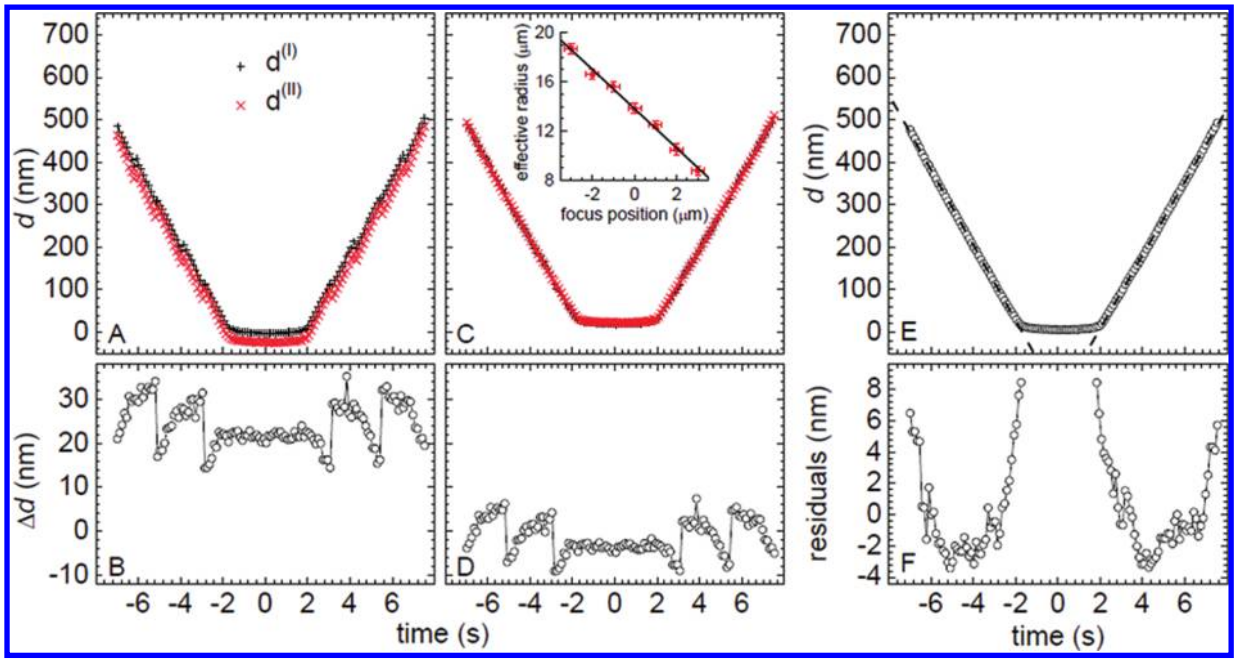

Figure 3. *R*-adjustment method. (A) Representative plot of the probe-surface distance vs time, reconstructed from a series of interferographs (λ = 543 nm) that were taken while a colloidal probe cantilever approached (decrease in d), contacted (plateau) and retracted (increase in d) from a glass surface in a solution of 10 mM NaCl in ultrapure water. $d^{(I)}$ (×) and $d^{(II)}$ (+) correspond to the distances calculated from two extrema of radially averaged intensity profiles (see Figure 2C) and the nominal probe radius R = 12.5 μm. (B) Corresponding plot of $\Delta d = d^{(I)}$-$d^{(II)}$ vs time. (C and D) The same data after minimization of $\chi^2 = \sum_t \Delta d(t)^2$ by adjustment of R (to 15.6 μm). The inset shows effective probe radii, determined according to the *R*-adjustment method for several measurements at different focus positions, with linear fit (solid line). (E) Plot of $d = [d^{(I)} + d^{(II)}]/2$ vs time. The apparent distance at "hard wall" approach is not zero. A mean distance at "hard wall" approach of 15 ± 5 nm was found for five different beads. Most likely, this systematic error is due to the simplified model and the surface roughness of the colloidal probe. To correct for the error, all data were offset by 15 nm. Dashed lines are linear fits to the approach and retract curves at distances >60 nm. (F) Residuals from the fits. The standard deviation is 3 nm.

response (which is 204 nm for λ = 543 nm). Close inspection of the data confirmed that the jumps in Δd at −5, −3, +3, and +5 s (Figure 3D) correlate with a transition to another fringe order. Apparently, these variations reflect limitations of the simple model. Fortunately, they largely disappear once $d^{(I)}$ and $d^{(II)}$ are averaged.

Figure 3E shows the distance d, obtained by averaging $d^{(I)}$ and $d^{(II)}$ after adjustment of R. It is notable that the apparent distance between the colloidal probe and the glass surface at hard-wall contact was significantly larger than zero. Additional measurements with a total of 5 different colloidal probes revealed a reproducible apparent distance of 15 ± 5 nm, even though parallel AFM measurements clearly indicated hard-wall contact. We believe that the overestimation of the distance originates in part from the simplified assumptions that underlie eq 1. Indeed Kühner and Sackmann[18] have previously found that a simple theory with similar assumptions overestimates the distances by 10 nm. The nm-scale roughness of the polystyrene beads is likely to be responsible for the remaining difference. To account for these systematic deviations, we have applied an offset of 15 nm to all distances determined by RICM. The *R*-adjusted data with 15 nm offset was then further used to compute force−distance curves, or to extract the absolute distance at closest approach.

The RICM response is inherently periodic, and distances can therefore be determined without ambiguity only within a range of $\lambda/2n$, or 204 nm for λ = 543 nm in water, unless additional information is available. In the example in Figure 3, we had used the knowledge about the approximate approach speed, v_{piezo}, and the fact that the colloidal probe must touch the bare glass surface at closest approach, to unambiguously reconstruct the distances over a range of more than 500 nm. This method fails if an approximate knowledge about the probe-glass distance at closest approach is not available. This is the case, for example, if a rather thick film of a priori unknown thickness (e.g., an HA film) is to be investigated. For a given wavelength, several distance−time curves that are offset in d by integer multiples of $\lambda/2n$ would be consistent with the data. To remedy this shortcoming, RICM images were acquired at two wavelengths simultaneously. By correlating the data at 438 and 543 nm, most of the potential solutions can be discarded, and a unique solution remains within a range of approximately 1 μm, as previously described in the literature.[19,20,42]

At large enough distances from the surface, the evolution of the bead position should be dictated by the constant approach and retract speed of the AFM (v_{piezo} = 100 nm/s). Straight lines indeed fitted the data at distances larger than 60 nm well (Figure 3E). The residuals (Figure 3F) revealed minor systematic deviations, which are likely due to limitations of the simple model used to calculate the heights.[18] The standard deviation over a distance range of 500 nm was 3 nm. The accuracy of our method in measuring relative distances over a large distance range is comparable to values reported with other RICM-based methods.[19,42] To obtain a measure of the resolving power of our setup, we performed sets of interferometric distance measurements with colloidal probes that were immobilized on a glass coverslip. The standard deviation for a given bead was typically smaller than 0.2 nm (data not shown), again

dx.doi.org/10.1021/la204602n | *Langmuir* 2012, 28, 3206−3216

similar to what is commonly reported,[18,19] although by an order of magnitude larger than in recent work by Heinrich et al.[21]

The absolute slopes, v_{tot}, of linear fits such as in Figure 3E were similar to v_{piezo}, but not always identical. They scattered significantly between measurements, even for measurements that were performed with the same setup at different times. These observations imply that, in addition to the actuation of the probe by the z-piezo, drifts contribute to probe−substrate distance variations. Thermal drift in the deflection of the AFM cantilever is readily detected by the AFM, and typically accounted only for a part of the discrepancy. We conclude that drifts of the position of the glass slide (and/or other components in the setup) do also affect the probe−surface distance. Discrepancies were typically within a few percent for the open fluid cell, but occasionally reached remarkable 30% for the closed fluid cell setup. Apparently, during approach and retract cycles, the silicone rubber seal of the AFM liquid cell exerts enough pressure to induce elastic deformation of the glass coverslip up to a few 100 nm. This type of drift cannot be detected by AFM alone, and would hence lead to erroneous force curves. It can, however, be readily detected and corrected by correlating AFM and RICM data, as we will outline in the following.

Determinaton of Force vs Absolute Distance Curves from AFM and RICM Data. It is worth noting that, in principle, force−distance curves can be extracted independently from RICM distance−time curves (Figure 3E) alone as well as from AFM deflection-displacement curves alone. In praxis, however, it proves useful to correlate both data sets, in order to be able to correct for drifts, to determine absolute distances and to maximize the resolution. Figure 4A and Table 1 define parameters that will be used in the description of the further data analysis process. Figure 4B displays a schematic force−distance curve that features three typical regimes of probe-sample interaction: a first regime in which the cantilever deflection is not affected by the sample ('noncontact'), a second regime in which probe-sample interactions result in cantilever deflection ("contact"), and a third regime in which the probe senses the rigid sample support ("hard-wall contact"). In practically relevant cases, the AFM data covers the noncontact and contact regimes, and optionally the hard-wall contact regime. The RICM data covers the repulsive regime, and optionally the noncontact and hard-wall contact regimes. Depending on whether or not the RICM data covers a sufficiently large part (i.e., spanning a range of several 100 nm in d) of the noncontact regime, different analysis strategies can be used to compute deflection vs distance curves. These are schematically outlined in Figure 4, panels C and D, and described in the following.

Case 1: RICM Data in the Noncontact Regime Is Available (Figure 4C). In the noncontact regime, the cantilever deflection δ is zero and the changes in displacement z and probe-substrate distance d are hence identical ($\Delta z = \Delta d$). The displacement rate v_{tot} can therefore be readily determined from the slope of a linear fit to the RICM distance-time data in this regime. RICM data are then easily converted into force−distance curves by a set of simple transformations (steps 1−3 in Figure 4C; in step 2, δ is offset to zero in the noncontact regime). Analysis of the AFM data is slightly more involved. First, the readout of the 4-quadrant photodetector voltage U_{PD} needs to be corrected for thermal drift in the cantilever deflection δ_{drift} (step 4). This is done by subtracting the slope in the noncontact regime from U_{PD}, followed by offsetting U_{PD} in the noncontact regime to zero. Second, the z-displacement is corrected for drifts in the cantilever deflection, δ_{drift}, and for drifts in the positioning of the glass slide relative to the probe, z_{drift}, according to $\Delta z = z_{piezo} + z_{drift} - \delta_{drift} = (v_{piezo} + v_{z\text{-}drift} - v_{c\text{-}drift})\Delta t = v_{tot}\Delta t$ (step 5), where v_{tot} is taken from the RICM data. Third, the drift-corrected deflection voltage U is converted into cantilever deflection through $\delta = US$ (step 8). In conventional AFM measurements, determination of the sensitivity S requires a separate reference measurement on a rigid substrate. If RICM data from the noncontact region is available, such a reference measurement is dispensable, because the RICM-derived force−distance curve can be used as an internal reference to determine sensitivity. To this end, AFM and RICM data are compared after simple transformations (steps 6−7). From δ (RICM data) and U (AFM data) at time t_1 (selected from data in the contact or hard-wall contact regimes) the sensitivity is given by $S = \delta(t_1)/U(t_1)$. Fourth, a simple transformation, based on $z = d-\delta$ and an appropriate offset in d provide deflection as a function of absolute distance (step 9). Here, the distance at closest approach, as determined by RICM, is used to offset d if data from the hard-wall contact regime is not available. Otherwise, the distance at closest approach is simply set to zero. Eventually, force vs absolute distance curves are obtained through $F(d) = k\delta(d)$ (step 10).

Case 2: RICM Data in the Noncontact Regime Is Not Available (Figure 4D). The data analysis is similar to case 1, but the analysis steps proceed in a different order (as indicated), and S and v_{tot} are determined in a different manner. S now needs to be provided via a separate reference measurement on a rigid substrate. v_{tot} is determined through an iterative procedure: starting with the estimate $\tilde{v}_{tot} = v_{piezo}$, $\tilde{v}_{tot}$ is adjusted through steps 4 and 5 until the deflections δ (from AFM data) and $\tilde{\delta}$ (from RICM data) coincide.

Two sets of representative AFM and RICM-derived force−distance curves, one with and another without hard-wall contact, are shown in Figure 5A. Overall, the AFM and RICM curves agree well. Most of the residual differences (Figure 5B) fall within a range of ±0.4 nN in F, or 4 nm in δ. This is close to the experimental error that we had established for the RICM data. Mildly increased residuals (up to 2 nN) were sometimes found at very small distances, the origin of which remains obscure. Increased data scatter, with a magnitude of 1 nN, can also be observed at distances above 500 nm in the RICM data. We suspect that this originates from the limited coherence of the employed light which makes the contrast of the interferographs decrease with increasing distance. We note that the resolution of the AFM in terms of relative distances and forces, as well as the distance range accessible to AFM, are superior to RICM. In praxis, it is hence preferable to make use of the AFM data, combined with a quantification of the distance at closest approach by RICM, to compute forces as a function of absolute distance.

Compression of HA Films. HA films were built on a streptavidin-coated supported lipid bilayer via a biotin anchor at one of the ends of the HA molecules (Figure 1B). Figure 6A shows a representative force−distance curve on such a grafted HA film. The interaction was purely repulsive. Both HA and polystyrene are negatively charged, and the absence of adhesion is hence not unexpected. In addition, the approach and retract curves superposed very well, indicating that the compression was purely elastic. The elastic response indicates (i) that the chains can rearrange rapidly, within seconds, without significant dissipative losses and regain their original conformation if external stress is released, and (ii) that concomitant liquid flow in and out of the compressed area occurs with relative ease,

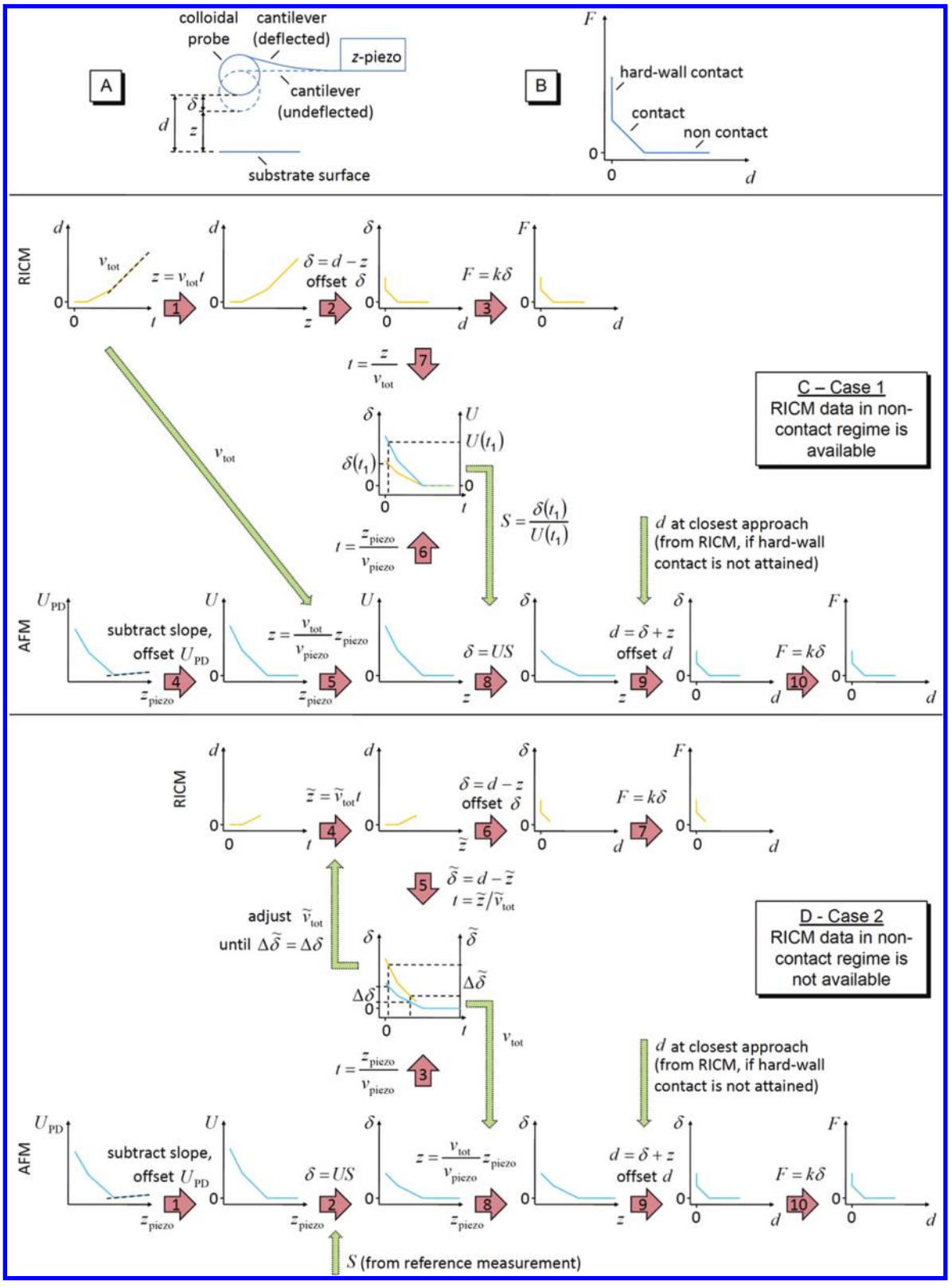

Figure 4. Process of determination of deflection-distance curves from RICM and AFM data. (A) Scheme of the setup with definition of parameters z, d and δ. (B) Scheme of an idealized force−distance curve with distinct noncontact, contact and hard-wall contact regimes. Each regime is represented by a straight line. (C and D) Idealized curves (RICM, orange lines; AFM, blue lines) are used to illustrate the data analysis process. (C) Case 1: If sufficient RICM data from the noncontact regime is available, then the accurate displacement rate v_{tot} can be determined from the slope of a linear fit to the data in this regime. The RICM data can then also be used as an internal reference to calibrate the sensitivity S. (D) Case 2: If sufficient RICM data from the noncontact regime is not available, then v_{tot} can be determined iteratively by correlating RICM and AFM deflection data. The sequence of data transformation steps is indicated by numbers inside the pink arrows. See Table 1 for the definition of additional parameters, and the main text for a detailed description of the analysis schemes.

dx.doi.org/10.1021/la204602n | *Langmuir* 2012, 28, 3206−3216

Table 1. Overview of Parameters Employed in Figure 4

Distance Parameters (in nm)	
probe-substrate distance	d
deflection	δ
(total) displacement	$z = d - \delta$
piezo-displacement	z_{piezo}
z-displacement drift	z_{drift}
cantilever deflection drift	δ_{drift}
Rate Parameters (in nm/s)	
total displacement rate	v_{tot}
z-piezo displacement rate	v_{piezo}
z-displacement drift rate	$v_{z\text{-drift}}$
cantilever deflection drift rate	$v_{c\text{-drift}}$
AFM Laser Detection Parameters	
sensitivity (in nm/V)	S
photodetector voltage (in V)	$U_{PD} = (\delta+\delta_{drift})/S$
deflection voltage (in V)	$U = \delta/S$
Force Parameters	
cantilever spring constant (in N/m)	k
force (in nN)	$F = k\delta$

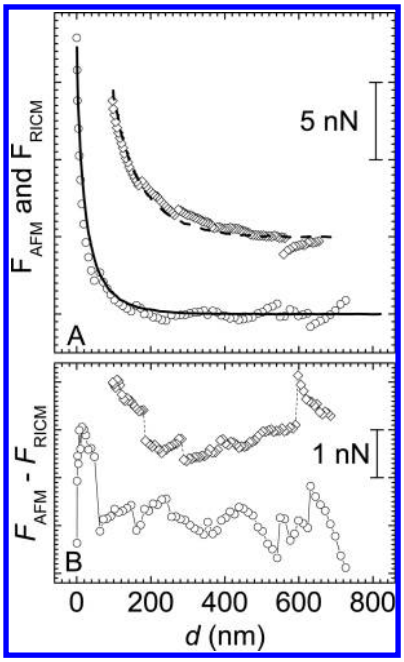

Figure 5. Comparison of force–distance curves by colloidal probe AFM and RICM. (A) Force–distance curves derived from AFM (lines) and RICM (symbols) data, respectively, acquired simultaneously during the approach of a colloidal probe to a bare glass surface in 10 μM NaCl (solid line, circles) and to an HA film (dashed line, lozenges, offset by 5 nN). RICM data were used to adjust the AFM data for linear drifts in probe-sample separation, to determine the AFM cantilever sensitivity (on bare glass) or the distance at closest approach (on the HA film). (B) Difference plots of the two sets of curves in panel A.

without significant energy dissipation. The force curves upon repeated compression of the same spot, and upon compression of different spots on the same sample, were highly reproducible (typically to within the line thickness in Figure 6). Independent measurements with different samples or probes also generated very similar curves, although with slightly larger deviations, which we attribute to minor variations in sample preparation.

Defining F_{th} = 50 pN, which is just above the noise level, as a threshold force, we estimated a film thickness of about

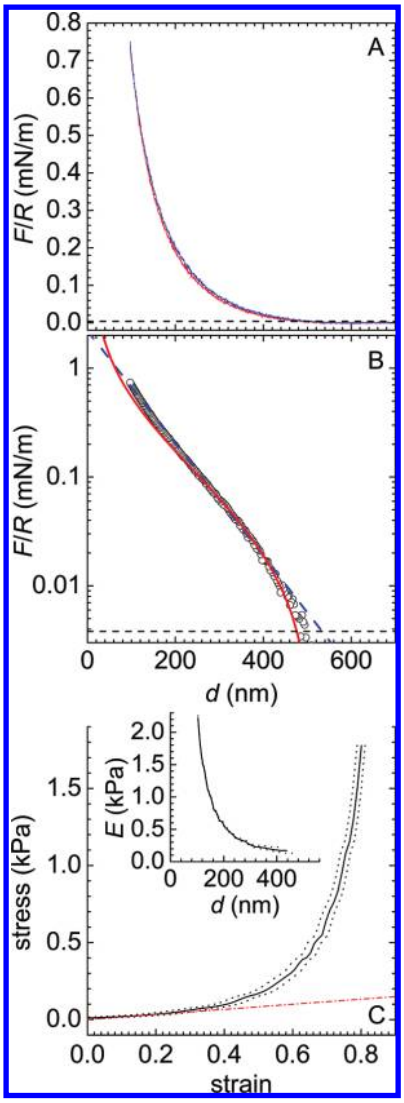

Figure 6. Compressive response of HA films. (A) Force vs distance curves (approach, red line; retract, blue line) for the compression of a film of end-grafted HA in the presence of 150 mM NaCl (Debye length 0.8 nm) at pH 7.4. Forces were normalized by the probe radius of 13.0 μm, obtained through the R-adjustment method at optimal focus position. (B) Approach data from A in a log–linear presentation (black circles) with fits from polymer brush models (eq 2A with L = 511 nm and s = 46 nm, red solid line; eq 2B with L = 501 nm and s = 50 nm, blue dashed line). Dashed horizontal lines indicate the threshold force F_{th}. (C) Stress vs strain curve for the approach data from A, assuming L = 518 ± 30 nm. Dotted curves represent the error due to the uncertainty in L. The slope of the red dash-dotted line (0.17 kPa) indicates the Young modulus, E = stress/strain, at low strain. The inset shows the evolution of E as a function of distance for strains above 0.15.

518 ± 30 nm from Figure 6A. This is about 6-fold more than the radius of gyration (R_g = 88 nm) and 6-fold less than the contour length (l_c = 2.86 μm) of 1.08 MDa HA.[20,43] The appreciable stretching of the grafted chains is a first indicator for the presence of a polymer brush. To test how well our film conforms to brush behavior, we compared the data with a simple model of neutral polymer brushes. For a single brush of equilibrium thickness L that is compressed between a planar and a spherical surface of radius $R \gg L$, scaling theory by Alexander and de Gennes[44] (AdG) predicts[23]

dx.doi.org/10.1021/la204602n | Langmuir 2012, 28, 3206–3216

$$\frac{F}{R} \cong \frac{8\pi}{35} kT \frac{L}{s^3}[7(L/d)^{5/4} + 5(d/L)^{7/4} - 12] \quad \text{for } d/L < 1 \tag{2A}$$

Here, $kT = 4.1 \times 10^{-21}$ J (at 25 °C) is the thermal energy and s the characteristic spacing between grafting points (i.e., s^2 is the surface area available per chain). According to the Derjaguin approximation, F/R is proportional to the compression energy $W = F/(2\pi R)$ between two planar surfaces, i.e. independent of the probe radius.[23] Within a rather large distance range, this equation can be approximated by an exponential[23]

$$\frac{F}{R} \cong 100 kT \frac{L}{s^3} e^{-2\pi d/L} \text{ for } 0.2 < d/L < 0.9 \tag{2B}$$

The right-hand side of both equations is accurate to within an unknown numerical prefactor of order unity.

Both equations fitted the experimental data well (Figure 6B). A fit with eq 2A over the range $0.5L \leq d \leq L$ resulted in L = 511 nm and s = 46 nm (Figure 6B). The thickness agrees well with the value that was directly extracted via F_{th} = 50 pN, and with a previously reported value of 530 ± 20 nm for a similarly prepared HA film.[20] In that study, we had also determined a mean anchor spacing of 60 nm on a hexagonal lattice, which corresponds to a characteristic spacing of $s = 3^{1/4}/2^{1/2} \times 60$ nm = 56 nm, by reflectometry. Here, the quantitative agreement is also reasonable, if one considers the uncertainty due to the unknown prefactor of order unity in eq 2. A fit with eq 2B gave L = 501 nm and s = 50 nm (Figure 6B), which is also in agreement with the above-mentioned values. The quality and the results of the fits provide further evidence that HA films behave as polymer brushes at physiological ionic strength.

Minor yet significant deviations were though noticeable at weak ($d > 0.9L$) and strong ($d < 0.5L$) compression. We suggest that these deviations come about because the Alexander-de Gennes model is a simplified representation of reality. For example, it neglects higher-order (e.g., ternary) interactions between chains, which may become important at high compression. It also assumes a constant density profile, rather than a more realistic gradually decaying density profile,[45−47] which is likely to affect the regime of weak compression. We noticed that L and s exhibited some sensitivity to the choice of the compression range: when the data at $d < 0.5L$ was included in the fit with eq 2A, L and s were about 13% smaller. The deviations at weak compression, on the other hand, had no appreciable effect on the fitting results. We remind also that HA is a charged polymer. A rigorous investigation of the impact of charge and density profile on HA brush behavior will be the object of a forthcoming publication. Here we confine us to note that at physiological ionic strength, the Debye length (0.8 nm) is much smaller than s, i.e. electrostatic interactions are short-ranged, and can be treated to good approximation as effective excluded volume interactions within the framework of polymer brush models.[48]

A few simple calculations shall illustrate the mechanical properties of the HA film. A material parameter of common interest, the Young modulus E, can be determined from the force vs distance curve in the following way. The pressure or stress acting on an HA film between two coplanar surfaces of distance d is given through Derjaguin's approximation as $P = dW/dd = (2\pi)^{-1} d(F/R)/dd$.[23] Stress as a function of strain, $1 - d/L$, is displayed in Figure 6C. To obtain meaningful derivatives of the force vs distance data, the curve was first smoothened by interpolation with a cubic B-spline algorithm. The Young modulus is given as the ratio of stress and strain, i.e. $E = P/(1 - d/L)$. It is approximately constant up to a compression of 25%, with a value of 0.17 kPa (Figure 6C, red dash-dotted line). For higher strains, E increases progressively, and reaches 2 kPa at 80% (Figure 6C, inset).

DISCUSSION

We have developed a novel method to determine forces between a colloidal probe and a planar surface as a function of their absolute distance. With this method we could quantify the compressive response of HA brushes under physiological ionic strength and pH conditions.

Instrumental Development. Our technical approach is based on the in situ combination of colloidal probe AFM and RICM. A purpose-designed algorithm for the analysis of RICM images provides absolute distances with an accuracy of a few nanometers. The technique is robust in several regards. First, and in contrast to methods described earlier,[19,28] the RICM image analysis method can correct for inaccuracies in probe radius and/or focus position. Second, linear drifts in the probe−sample distance can be detected and corrected for. Third, the sensitivity of the AFM deflection detection can in some cases (i.e., when RICM data for the noncontact regime is available) be calibrated without a separate reference measurement on a bare surface.

In the past, the surface force apparatus (SFA),[22,49,50] has been very successful for the investigation of forces between surfaces. A comparison with our setup is worthwhile. With a force resolution of the AFM of about 10 pN and typical bead radii above 10 μm, the resolution of our setup in terms of normalized normal force is $F/R \approx 1$ μN/m. This value is comparable to the best force resolution that can be obtained by SFA.[22,51] The current resolution in d remains by one to 2 orders of magnitude below that of the SFA.[22] Further refinements in the data analysis[18,19,21] might improve this value somewhat, but ultimately the nm-scale roughness of the colloidal bead and the surface will present limitations that currently remain hard to overcome. On the other hand, the combined AFM/RICM setup has practical advantages: the setup can be readily implemented on commercially available combinations of AFM and optical microscopy; and the chamber volume is approximately 200 μL, or about 2 orders of magnitude less than the SFA, which is desirable if the amount of available sample is limited.

The combined AFM/RICM setup should in the future prove useful to investigate soft and solvated transparent films of thicknesses between a few 10 nm and a few micrometers. The method is versatile. The planar surface and the colloidal probe can be functionalized independently, and the interaction between two surfaces with different adlayers can readily be probed. The approach rates accessible by AFM are typically faster than those of the SFA, and our setup should hence be particularly useful to investigate compression dynamics out of equilibrium. With the sensitivity of AFM to cantilever torque, the AFM/RICM combination can also be used to study the friction between polymer films as a function of normal load.

Mechanical Properties of Hyaluronan Films: Biological Implications. Hyaluronan is produced and extruded into the extracellular space by hyaluronan synthases, and it is known that the glycosaminoglycan can stay attached with one of its ends to these cell surface membrane proteins. Our model films recapitulate this mode of attachment. From L = 518 nm and s = 56 nm, we find that the film has a remarkable hydration

of ∼99.9% and a mean HA concentration of 1.1 mg/mL.[20] Similar concentrations have been found in vivo, e.g., in synovial fluid.[52] Indeed, HA has been proposed to adopt a brush-like conformation around cells, in different topologies.[1,53−55] Our results may hence have direct relevance for the mechanical properties of the cellular environment of, e.g., chondrocytes in cartilage[53] or of the endothelial cell surface.[56−58] They should present an interesting reference for future mechanical studies on real cellular coats, which are likely to be more complex.[55,59]

To our knowledge, this is the first study on the mechanical properties of films of (end-)grafted HA chains. The Young moduli of our HA brushes, 0.2 to 2 kPa, are representative for very soft gels. A 0.4% agarose gel, for example, has a Young modulus of approximately 1 to 2 kPa.[60] From a polymer physics point of view,[6,7,44,61] the behavior of HA brushes is expected to be drastically different from HA chains that are physisorbed, specifically bound or covalently attached via several points along the chain, as investigated in earlier studies.[24,38,62−64] More specifically, the latter are expected to exhibit a thickness comparable to the radius of gyration whereas brushes can become much thicker. Indeed, the thickness of our HA brushes is 5 to 10-fold larger than what has been reported previously for side-attached HA-films of similar molecular weight under near-physiological ionic strength.[38,62,64]

The colloidal probes that we have used in this study are large enough to interact with many chains simultaneously. For example, if the film is compressed to a strain of 0.8, the contact area would cover about 10 000 HA chains, as can be easily estimated from s and R. With HA-rich pericellular coats being present around a large number of cell types, one might expect that such coats perturb the imaging of the cell surface by mechanical techniques such as AFM.[65] The size of the probes that are typically used for imaging, however, are much smaller than what we have used here. Rescaling our results (Figure 6) to a probe radius of 25 nm, we can estimate that a force of 50 pN, comparable to the forces that are typically used for AFM imaging, would suffice to achieve 90% compression. In fact, it is likely that the compression forces are even smaller, because the sharp imaging probes interact with a rather small number of chains (e.g., a few 100 for a cone-shaped tip with 70° opening angle) and these can evade compression by bending to the side.[66] This rationalizes why imaging of cell surfaces can be possible despite the presence of a thick pericellular coat.

We remind that our HA brushes were formed on fluid supported lipid bilayers, and one might argue that the compression should result in the lateral displacement of HA out of the compression zone. This has indeed been reported for films of HA molecules that were either physisorbed to surfaces[63] or covalently bound to SLBs via multiple attachment points along the chain.[62] The good agreement of our data with polymer brush models suggests that lateral displacement is negligible in our case. The reason is likely to lie in the details of our experimental approach. First, we used streptavidin to graft HA to the SLB. This protein is known to form two-dimensional crystalline domains on glass-SLBs.[67] Some, if not all, of the HA anchor points are hence likely to be immobile. Second, the approach speed in our study was rather high, compared to previous SFA-based studies.[62,63] The lateral disentanglement of HA chains in the brush might hence be significantly slower than the compression in our case.

Future studies that systematically vary the grafting density, molecular weight and lateral mobility of HA, external conditions such as divalent ions or pH, and the compression rate should allow to further refine our understanding of the behavior of HA assemblies in and out of equilibrium. Our study illustrates that the experimental data for such a system can be quantitatively compared with predictions from polymer theory. The complexity of the studied system can now be systematically increased by including other macromolecules of interest, such as hyaladherins.[36]

■ CONCLUSIONS

We have developed a novel method, based on the in situ combination of colloidal probe AFM and RICM that enables to probe the compression forces, and potentially even friction forces, of surface-confined polymer films with tight control on the distance between the two surfaces. The two techniques are highly complementary: AFM provides forces as a function of relative distance with high resolution; RICM supplies absolute distances, enables the correction of AFM data for linear instrumental drifts, and can even give cantilever sensitivity without an extra reference measurement. The method was used to investigate the compressive response of films of end-grafted HA. The films showed a compressive response in good quantitative agreement with a simple theoretical model of polymer brushes. The method represents a novel tool for the quantitative correlation between the supramolecular organization and the mechanical properties of surface-confined HA assemblies, and highly solvated polymer films such as polymer brushes in general.

■ AUTHOR INFORMATION

Corresponding Author

*E-mail: rrichter@cicbiomagune.es.

■ ACKNOWLEDGMENTS

This work was funded by the Department of Industry of the Basque Government (Program ETORTEK), the Spanish Ministry of Science and Innovation (MICINN, refs MAT2008-04192 and RYC2009-04275) and the German Federal Ministry of Education and Research (BMBF, ref 0315157).

■ REFERENCES

(1) Evanko, S. P.; Tammi, M. I.; Tammi, R. H.; Wight, T. N. *Adv. Drug Delivery Rev.* **2007**, *59*, 1351−65.
(2) Charnley, M.; Textor, M.; Acikgoz, C. *React. Funct. Polym.* **2011**, *71*, 329−34.
(3) Chen, M.; Briscoe, W. H.; Armes, S. P.; Klein, J. *Science* **2009**, *323*, 1698−701.
(4) Ren, K.; Crouzier, T.; Roy, C.; Picart, C. *Adv. Funct. Mater.* **2008**, *18*, 1378−89.
(5) Senaratne, W.; Andruzzi, L.; Ober, C. K. *Biomacromolecules* **2005**, *6*, 2427−48.
(6) Fleer, G. J.; Stuart, M. A. C.; Scheutjens, J. M. H. M.; Cosgrove, T.; Vincent, B. *Polymers At Interfaces*; Chapman & Hall: London, UK, 1993.
(7) Rubinstein, M.; Colby, R. H. *Polymer Physics*; Oxford University Press: Oxford, U.K., 2003.
(8) Butt, H. J. *Biophys. J.* **1991**, *60*, 1438−44.
(9) Ducker, W. A.; Senden, T. J.; Pashley, R. M. *Nature* **1991**, *353*, 239−41.
(10) Butt, H.-J.; Cappella, B.; Kappl, M. *Surf. Sci. Rep.* **2005**, *59*, 1−152.
(11) Dimitriadis, E. K.; Horkay, F.; Maresca, J.; Kachar, B.; Chadwick, R. S. *Biophys. J.* **2002**, *82*, 2798−810.
(12) Feiler, A.; Plunkett, M. A.; Rutland, M. W. *Langmuir* **2003**, *19*, 4173−9.
(13) Engler, A. J.; Richert, L.; Wong, J. Y.; Picart, C.; Discher, D. E. *Surf. Sci.* **2004**, *570*, 142−54.

(14) Picart, C.; Lavalle, P.; Hubert, P.; Cuisinier, F. J. G.; Decher, G.; Schaaf, P.; Voegel, J.-P. *Langmuir* **2001**, *17*, 7414−24.
(15) Dean, D.; Han, L.; Grodzinsky, A. J.; Ortiz, C. *J. Biomech.* **2006**, *39*, 2555−65.
(16) Clark, S. C.; Walz, J. Y.; Ducker, W. A. *Langmuir* **2004**, *20*, 7616−22.
(17) Rädler, J.; Sackmann, E. *Langmuir* **1992**, *8*, 848−53.
(18) Kühner, M.; Sackmann, E. *Langmuir* **1996**, *12*, 4866−76.
(19) Limozin, L.; Sengupta, K. *ChemPhysChem* **2009**, *10*, 2752−68.
(20) Richter, R. P.; Hock, K. K.; Burkhartsmeyer, J.; Boehm, H.; Bingen, P.; Wang, G.; Steinmetz, N. F.; Evans, D. J.; Spatz, J. P. *J. Am. Chem. Soc.* **2007**, *129*, 5306−7.
(21) Heinrich, V.; Wong, W. P.; Halvorsen, K.; Evans, E. *Langmuir* **2008**, *24*, 1194−203.
(22) Israelachvili, J.; Min, Y.; Akbulut, M.; Alig, A.; Carver, G.; Greene, W.; Kristiansen, K.; Meyer, E.; Pesika, N.; Rosenberg, K.; Zeng, H. *Rep. Prog. Phys.* **2010**, *73*, 036601.
(23) Israelachvili, J. N. *Intermolecular and Surface Forces*, 2nd ed.; Academic Press: New York, 1991.
(24) Seror, J.; Merkher, Y.; Kampf, N.; Collinson, L.; Day, A. J.; Maroudas, A.; Klein, J. *Biomacromolecules* **2011**, *12*, 3432−43.
(25) Hlady, V.; Pierce, M.; Pungor, A. *Langmuir* **1996**, *12*, 5244−6.
(26) Stuart, J. K.; Hlady, V. *Biophys. J.* **1999**, *76*, 500−8.
(27) Dubreuil, F.; Elsner, N.; Fery, A. *Eur. Phys. J. E* **2003**, *12*, 215−21.
(28) Robert, P.; Sengupta, K.; Puech, P.-H.; Bongrand, P.; Limozin, L. *Biophys. J.* **2008**, *95*, 3999−4012.
(29) Erath, J.; Schmidt, S.; Fery, A. *Soft Matter* **2010**, *6*, 1432−7.
(30) Toole, B. P. *Nat. Rev. Cancer* **2004**, *4*, 528−39.
(31) Russell, D. L.; Salustri, A. *Semin. Reprod. Med.* **2006**, *24*, 217−27.
(32) Toole, B. P. *Semin. Cell Dev. Biol.* **2001**, *12*, 79−87.
(33) Cleland, R. L.; Wang, J. L.; Detweiler, D. M. *Macromolecules* **1982**, 15.
(34) Knudson, W.; Knudson, C. B. *J. Cell Sci.* **1991**, *99*, 227−35.
(35) Day, A. J.; de la Motte, C. A. *Trends Immunol.* **2005**, *26*, 637−43.
(36) Baranova, N. S.; Nilebäck, E.; Haller, F. M.; Briggs, D. C.; Svedhem, S.; Day, A. J.; Richter, R. P. *J. Biol. Chem.* **2011**, *286*, 25675−86.
(37) Ploem, J. S. *Mononuclear Phagocytes in Immunity, Infection and Pathology*; Von Furth, R., Ed.; Blackwell: Oxford, U.K. 1975; pp 405−21.
(38) Wolny, P. M.; Banerji, S.; Gounou, C.; Brisson, A. R.; Day, A. J.; Jackson, D. G.; Richter, R. P. *J. Biol. Chem.* **2010**, *285*, 30170−80.
(39) Hutter, J. L.; Bechhoefer, J. *Rev. Sci. Instrum.* **1993**, *64*, 1868−73.
(40) Richter, R. P.; Mukhopadhyay, A.; Brisson, A. *Biophys. J.* **2003**, *85*, 3035−47.
(41) Eisele, N. B.; Frey, S.; Piehler, J.; Gorlich, D.; Richter, R. P. *EMBO Rep.* **2010**, *11*, 366−72.
(42) Schilling, J.; Sengupta, K.; Goennenwein, S.; Bausch, A. R.; Sackmann, E. *Phys. Rev. E* **2004**, *69*, 021901.
(43) Takahashi, R.; Kubota, K.; Kawada, M.; Okamoto, A. *Biopolymers* **1999**, *50*, 87−98.
(44) de Gennes, P. G. *Adv. Colloid Interface Sci.* **1987**, *27*, 189−209.
(45) Milner, S. T. *Science* **1991**, *251*, 905−14.
(46) Zhulina, E. B.; Borisov, O. V.; Priamitsyn, V. A. *J. Colloid Interface Sci.* **1990**, *137*, 495−511.
(47) Zhulina, E. B.; Priamitsyn, V. A.; Borisov, O. V. *Polym. Sci. U.S.S.R.* **1989**, *31*, 205−16.
(48) Pincus, P. *Macromolecules* **1991**, *24*, 2912−9.
(49) Israelachvili, J. N.; McGuiggan, P. M. *J. Mater. Res.* **1990**, *5*, 2223−31.
(50) Klein, J. *J. Chem. Soc., Faraday Trans. 1* **1983**, *79*, 99−118.
(51) Briscoe, W. H.; Horn, R. G. *Langmuir* **2002**, *18*, 3945−56.
(52) Fraser, J. R.; Laurent, T. C.; Laurent, U. B. *J. Intern. Med.* **1997**, *242*, 27−33.
(53) Cohen, M.; Joester, D.; Geiger, B.; Addadi, L. *ChemBioChem* **2004**, *5*, 1393−9.
(54) Rilla, K.; Tiihonen, R.; Kultti, A.; Tammi, M.; Tammi, R. *J. Histochem. Cytochem.* **2008**, *56*, 901−10.
(55) Sokolov, I.; Iyer, S.; Subba-Rao, V.; Gaikwad, R. M.; Woodworth, C. D. *Appl. Phys. Lett.* **2007**, *91*, 023902.
(56) Nijenhuis, N.; Mizuno, D.; Schmidt, C. F.; Vink, H.; Spaan, J. A. E. *Biomacromolecules* **2008**, *9*, 2390−8.
(57) Nijenhuis, N.; Mizuno, D.; Spaan, J. A.; Schmidt, C. F. *Phys. Biol.* **2009**, *6*, 025014.
(58) Weinbaum, S.; Zhang, X.; Han, Y.; Vink, H.; Cowin, S. C. *Proc. Natl. Acad. Sci. U.S.A.* **2003**, *100*, 7988−95.
(59) Boehm, H.; Mundinger, T. A.; Boehm, C. H. J.; Hagel, V.; Rauch, U.; Spatz, J. P.; Curtis, J. E. *Soft Matter* **2009**, *5*, 4331−7.
(60) Frey, S.; Richter, R. P.; Görlich, D. *Science* **2006**, *314*, 815−7.
(61) Netz, R. R.; Andelman, D. *Phys. Rep.* **2003**, *380*, 1−95.
(62) Benz, M.; Chien, N.; Israelachvili, J. N. *J. Biomed. Mater. Res.* **2004**, *71A*, 6−15.
(63) Tadmor, R.; Chen, N.; Israelachvili, J. N. *Macromolecules* **2003**, *36*, 9519−26.
(64) Albersdörfer, A.; Sackmann, E. *Eur. Phys. J. B* **1999**, *10*, 663−72.
(65) Le Grimellec, C.; Lesniewska, E.; Cachia, C.; Schreiber, J. P.; de Fornel, F.; Goudonnet, J. P. *Biophys. J.* **1994**, *67*, 36−41.
(66) O'Shea, S. J.; Welland, M. E.; Rayment, T. *Langmuir* **1993**, *9*, 1826−35.
(67) Richter, R. P.; Brisson, A. *Langmuir* **2003**, *19*, 1632−40.